ISSN: 2641-2039
DOI: 10.33552/GJES.2026.12.000795
Global Journal of Engineering Sciences
Iris Publishers

Research Article

Copyright © All rights are reserved by Yanzi Yu

Tensile Localisation and Interfacial Load Transfer in Textile-Reinforced Geopolymer Composites: An Extended Finite Element Analysis

Xiaowei Wang[1], Jiahao Li[2], Liankun Wang[1], Jiong Zhang[1], and Yanzi Yu[3*]

[1]*School of Civil Engineering and Architecture, Wuyi University, Jiangmen, Guangdong 529020, China*

[2]*P&T Architects and Engineers Ltd, Hong Kong HKG999077, China*

[3]*School of Humanities, Political Science and Law, Wuyi University, Jiangmen 529020, China*

***Corresponding author:** Yanzi Yu, School of Humanities, Political Science and Law, Wuyi University, Jiangmen 529020, China.

Received Date: October 23, 2026

Published Date: November 12, 2026

Abstract

The tensile response of textile-reinforced geopolymer composites depends on matrix inelasticity, textile bridging and interfacial load transfer. Comparable peak loads can arise from different localisation mechanisms. This study uses an extended finite element framework to examine carbon, normal-steel and tight-weave-steel textile architectures, comparing the numerical responses with published experimental reference curves. The assessment considers load–elongation curves, reported PEEQ fields in geopolymer and mortar matrices, and the tensile damage variable DAMAGET in geopolymer composites. Values recovered from the plotted curves give peak-load differences of a few percent across six cases, although discrepancies along the post-peak branches vary with architecture. The displayed PEEQ extrema span approximately one order of magnitude, while the DAMAGET extrema for the three geopolymer systems range from 0.3709 to 0.3752. These outputs describe different constitutive quantities. Neither directly identifies crack paths or dissipated energy, and they cannot be used interchangeably. Assessing textile architecture therefore requires attention to the location and spatial organisation of localisation, together with interfacial constraints. Peak load and contour colour alone are insufficient. This approach distinguishes structural agreement from evidence of a local failure mechanism and supports a mechanics-based interpretation of the simulations.

Keywords: Geopolymer Composites; Textile Reinforcement; XFEM; Interfacial Transfer; Localisation; Tensile Damage

Abbreviations: ACK, Aveston–Cooper–Kelly; CDP, concrete damaged plasticity; EGC, engineered geopolymer composite; FE, finite element; PEEQ, Abaqus equivalent plastic strain output identifier; PEEQT, Abaqus tensile equivalent plastic strain output identifier; DAMAGET, Abaqus tensile damage variable; TR-EGC, textile-reinforced engineered geopolymer composite; TRM, textile-reinforced mortar; XFEM, extended finite element method.

Introduction

Tensile load transfer in textile-reinforced quasi-brittle composites couples the structural force carried by the matrix and textile with local concentrations of cracking, slip and stiffness degradation. Textile bridging can sustain load after matrix cracking. How that load redistributes over the gauge region depends on textile architecture, matrix deformability and interfacial constraint. ACK-type multiple-fracture theory describes the competition between matrix cracking and fibre load carrying. Fracture-mechanics

This work is licensed under Creative Commons Attribution 4.0 License

analyses also show how interfacial bonding and frictional sliding affect matrix cracking [1,2]. These theories guide interpretation of load transfer, but the local fields still need to be examined for each textile system.

Engineered geopolymer composites use dispersed-fibre bridging to improve matrix tensile deformability. Their design depends on matching matrix fracture resistance with fibre-bridging capacity [3,4]. A continuous textile grid adds load-transfer paths among the matrix, dispersed fibres and textile. Reviews of experimental studies show that specimen geometry, gripping and strain measurement affect first cracking, hardening and post-peak response in textile-reinforced cementitious composites [5]. Geopolymer composition and curing also influence the constitutive response [6]. Comparisons of textile architectures must therefore keep material stress, specimen-level nominal stress and structural force distinct.

A numerical model must account for local displacement discontinuities and relative slip between textile and matrix. The partition-of-unity method admits enrichment functions based on the problem being modelled [7]. XFEM uses this construction to separate crack geometry from the background mesh [8]. A traction–separation relation describes interfacial debonding and dissipation separately; related approaches have been applied to textile-reinforced mortar [9,10]. Even with these descriptions, different local damage distributions can yield similar load–elongation curves. Peak-load agreement alone cannot resolve this non-uniqueness or its implications for the failure mechanism.

This study examines how textile architecture affects the spatial organisation of inelastic deformation and tensile damage when structural tensile responses are comparable. The numerical results cover carbon, normal-steel and tight-weave-steel architectures, using published tensile experiments as the reference [11]. The assessment begins with six load–elongation responses, then considers the reported PEEQ fields in geopolymer and mortar systems and the DAMAGET fields in geopolymer systems. Structural agreement, local constitutive outputs and crack geometry are examined as distinct forms of evidence when interpreting the effects of architecture on load transfer and localisation.

Materials and Methods

Material systems and loading

The specimens use carbon (C), normal-steel (S) or tight-weave-steel (TS) textiles. TR-EGC denotes the geopolymer systems, and TRM denotes the mortar controls. Structural comparisons cover C-4, S-4, TS-4, C-8, S-8 and TS-8; the numeral denotes the alkali-solution concentration group in mol/L. The finite element curves and fields are assessed against the tensile experiments reported by Lam and co-workers [11]. Figure 1 shows the specimen, textile arrangement and end loading. Load is applied through a reference point at one end, with rigid-body motion restrained at the other. The clamping and central deformation regions are considered separately in the local-field analysis.

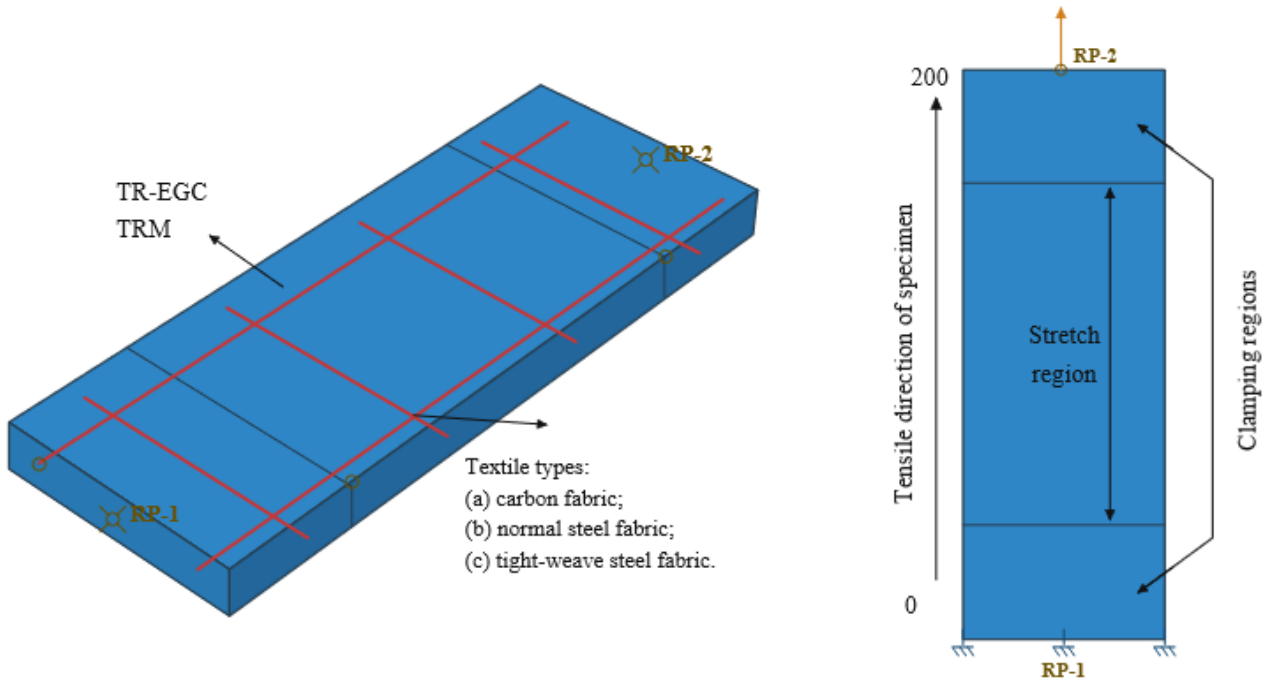


Figure 1: Specimen, textile arrangement and end loading. TR-EGC and TRM denote the matrix systems; RP-1 and RP-2 are end reference points. The schematic does not specify the extensometer gauge length used for the supplementary response.

The structural assessment compares force P and elongation Δ directly, without converting them using a cross-sectional area or gauge length. This preserves quantities that are directly comparable between experiment and computation. Appendix A defines textile material stress and S-4 specimen nominal stress separately. Because these measures use different denominators, their peaks cannot be compared as the same stress quantity.

Displacement discontinuities and crack-surface traction

Equation (1) gives a small-strain displacement approximation enriched to represent a jump across the crack surface. N denotes a shape function, u denotes a conventional nodal degree of freedom, a denotes a jump-enrichment degree of freedom, and J denotes the set of enriched nodes. The shifted Heaviside function is zero at the associated node, keeping enrichment amplitudes distinct from conventional nodal displacements. The expression uses the established XFEM approximation space [8]; it does not introduce a new enrichment algorithm.

$$\mathbf{u}^h(\mathbf{x}) = \sum_{i\in I} N_i(\mathbf{x})\mathbf{u}_i + \sum_{j\in J} N_j(\mathbf{x})[H(\varphi(\mathbf{x})) - H(\varphi(\mathbf{x}_j))]\mathbf{a}_j \quad (1)$$

Stationary linear-elastic cracks with near-tip asymptotic enrichment have different approximation requirements from propagating cracks represented by cohesive segments or phantom nodes. The Abaqus implementation for propagating cohesive cracks uses the displacement jump and does not require stationary-crack singular enrichment [12]. Equations (1)–(2) therefore focus on displacement discontinuities and crack-surface transfer. Material-point outputs describe the constitutive response, while crack-specific outputs describe crack geometry. These outputs provide distinct information.

Equation (2) sets out the virtual-work contributions to load transfer. Ω denotes the bulk domain, Γc the internal matrix crack surfaces, Γi the textile–matrix interfaces and Γt the external traction boundary. Matrix cracks and material interfaces are physically distinct, so their traction contributions cannot be represented by an interchangeable damage variable. The expression also makes clear that total reaction and displacement alone do not uniquely determine the separate contributions of crack-surface and interface dissipation.

$$\int_\Omega \boldsymbol{\sigma}:\delta\boldsymbol{\varepsilon}\mathrm{d}\Omega + \int_{\Gamma_c}\mathbf{t}_c\cdot\delta[\![\mathbf{u}]\!]\mathrm{d}\Gamma + \int_{\Gamma_i}\mathbf{t}_i\cdot\delta[\![\mathbf{u}]\!]\mathrm{d}\Gamma = \int_{\Gamma_t}\bar{\mathbf{t}}\cdot\delta\mathbf{u}\mathrm{d}\Gamma \quad (2)$$

Interfacial softening and the energy scale

A traction–separation relation links relative displacement between textile and matrix to the interfacial force. Equation (3) defines a scalar bilinear relation for monotonic opening: K is the initial interface stiffness, t0 the peak traction, and δ0 and δf the separations at the onset of softening and at complete failure. Compressive contact and tangential transfer need separate descriptions. Interface models for textile-reinforced mortar provide a basis for these relations, although the parameters remain specific to each textile–matrix system [10].

$$t(\delta) = \begin{cases} K\delta & 0 \le \delta \le \delta_0 \\ t_0\frac{\delta_f-\delta}{\delta_f-\delta_0} & \delta_0 < \delta \le \delta_f \\ 0 & \delta \ge \delta_f \end{cases} \quad (3)$$

$$\delta_0 = \frac{t_0}{K}$$

For the bilinear relation, the area under the traction–separation curve gives the dissipation per unit area, as shown in Eq. (4). Peak traction and failure separation jointly determine this energy. Peak structural force alone cannot identify them separately. Strain softening in a quasi-brittle bulk material also needs a characteristic-length treatment to preserve physical fracture energy after discretisation [9,13]. Both the energy and discretisation scales therefore constrain the interpretation of local fields and structural curves.

$$G_I = \int_0^{\delta_f} t(\delta)\mathrm{d}\delta = \frac{1}{2}t_0\delta_f \quad (4)$$

Constitutive meaning of the field outputs

DAMAGET is the tensile damage variable dt. For uniaxial tension, Eq. (5) relates damaged stress to effective undamaged stress. The variable dt describes stiffness degradation, not crack opening, cracked-area fraction or dissipated energy. A value below unity does not by itself establish whether a crack has traversed the specimen [14]. Damage variables for material interfaces and cohesive crack surfaces must also be distinguished from this bulk-material output.

$$\sigma_t = (1-d_t)\overline{\sigma_t}, 0 \le d_t \le 1 \quad (5)$$

PEEQ is used here as a software output identifier; its physical meaning depends on the material model. In concrete damaged plasticity, PEEQ is the compressive equivalent plastic strain, while PEEQT identifies the tensile equivalent plastic strain [14]. The displayed PEEQ field therefore cannot be labelled as tensile cracking strain or used on its own to trace an XFEM crack. It is used to compare non-uniform material responses at the displayed output states. Its distribution is interpreted separately from DAMAGET.

Assessment of structural responses and local fields

The structural comparison follows the initial response, the region near the peak and the post-peak branch. Equation (6) defines the peak-load difference, with superscripts num and exp denoting the numerical response and experimental reference. Table 1 values are estimated from recovered graphical coordinates and describe agreement between the plotted curves. They do not have the precision of the original sampling records. Across the cases, one vertical pixel represents approximately 0.04–0.12 kN. Differences below that resolution are not used to rank model performance.

$$e_P = 100\left(\frac{P_{\max}^{\mathrm{num}}}{P_{\max}^{\mathrm{exp}}} - 1\right)\% \quad (6)$$

The local-field assessment reports each variable identifier together with its colourbar extremum and the location of elevated values. Each panel has its own numerical scale, so the same colour can represent different values. The fields show spatial snapshots at the displayed output states, not maxima over the full loading history. The cases are also not assumed to be at the same displacement or dissipation stage. These snapshots support an assessment of spatial localisation, but they do not determine crack-growth rates or energy partition.

Results and Discussion

Load–elongation responses

Figure 2 compares the experimental reference curves with the finite element curves for the six specimen groups. All systems show changes in stiffness and a nonlinear load-carrying stage, with differences in the hardening interval and post-peak unloading. The tight-weave-steel cases carry higher forces in these comparisons, while the normal-steel cases have lower peaks. These are specimen-level responses. An intrinsic material advantage cannot be inferred without accounting for textile content, matrix behaviour and interface conditions.

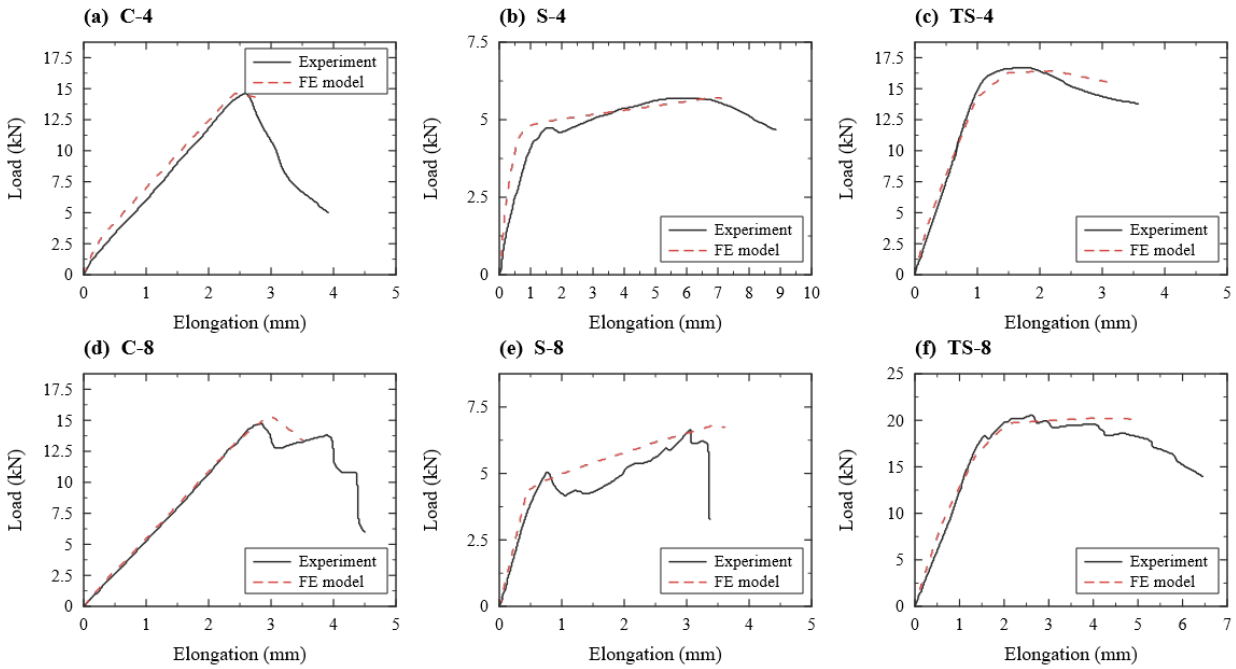


Figure 2: Experimental reference and finite element load–elongation curves: (a) C-4; (b) S-4; (c) TS-4; (d) C-8; (e) S-8; (f) TS-8. The experimental reference is [11]; the finite element curves are the numerical results of this study. The curves use recovered graphical coordinates without smoothing.

Table 1: Peak-load estimates and relative differences from the plotted curves.

Case	Experimental peak (kN)	Numerical peak (kN)	Difference (%)
C-4	14.6	14.6	≈0
S-4	5.7	5.7	≈0
TS-4	16.7	16.4	−1.6
C-8	14.8	15.2	+3.3
S-8	6.6	6.8	+2.2
TS-8	20.5	20.2	−1.5

Peak loads are reported to 0.1 kN, while differences are calculated from unrounded recovered coordinates. Approximately zero indicates a difference below one vertical pixel, not zero model error.

Table Abbreviations: C, carbon textile; S, normal-steel textile; TS, tight-weave-steel textile; 4 and 8, alkali-solution concentration groups in mol/L; kN, kilonewton.

The estimated relative peak differences range from approximately −1.6% to +3.3% (Table 1). For C-4 and S-4, the differences are smaller than one vertical pixel; near-zero percentages therefore do not imply high-precision validation. C-8 and S-8 have positive peak differences, while TS-4 and TS-8 have negative differences. A single amplitude correction cannot account for all architectures. The numerical branches also fail to reproduce the full extent of the post-peak declines or local unloading in C-4, C-8 and S-8. Agreement near the peak thus leaves the softening mechanism unresolved.

The structural reaction combines contributions from several local load-transfer paths and can mask trade-offs among slip, stress concentration and the spread of damaged regions. Different combinations of interface and matrix-softening parameters may give similar peaks but different post-peak paths. The force curves are therefore used to check the structural response. The field analysis adds constraints to the local interpretation; it does not provide an interchangeable form of validation.

Spatial non-uniformity of the PEEQ fields

Figure 3 compares the PEEQ fields for the three textiles in TR-EGC and TRM. Carbon-textile TR-EGC has two concentrated regions of elevated values near the specimen centre. These regions are smaller in normal-steel TR-EGC, while tight-weave-steel TR-EGC has several separated central regions. Both the distributions and amplitudes change in the TRM counterparts. Because the panels use different scales, spatial patterns and numerical magnitudes must be assessed separately.

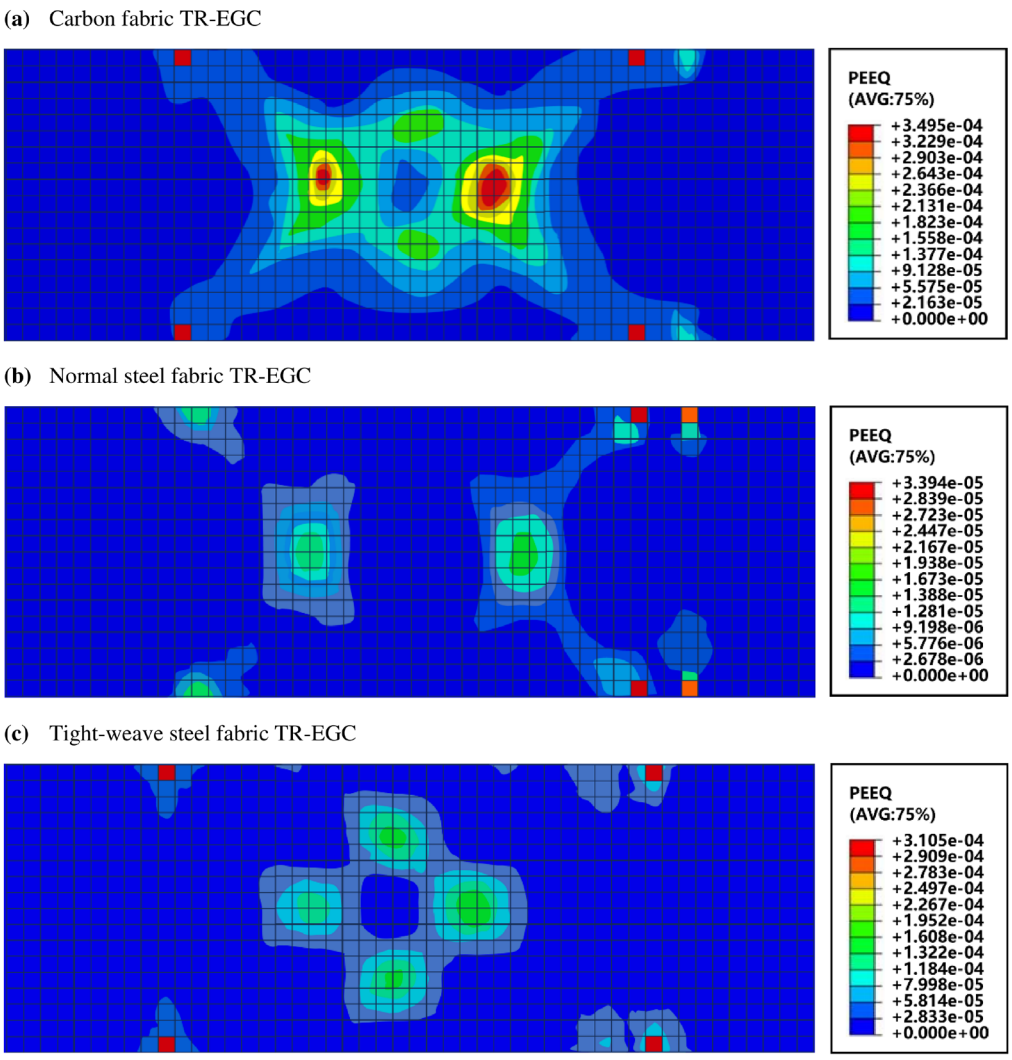


Figure 3: PEEQ fields from the simulations. Panels (a–c): carbon, normal-steel and tight-weave-steel TR-EGC. Each panel retains its own numerical colourbar and nodally averaged display. See 'Constitutive meaning of the field outputs' for the interpretation of PEEQ; these fields do not directly identify crack paths.

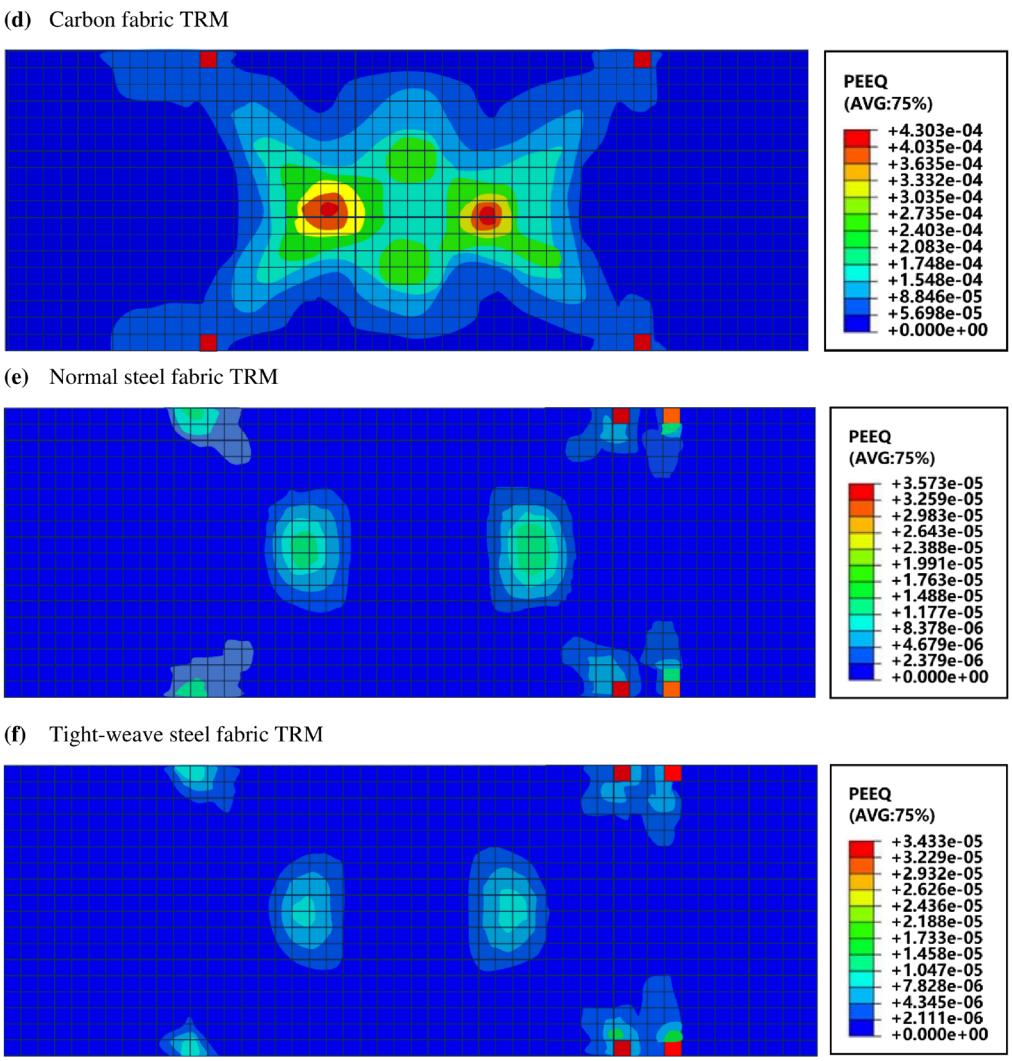


Figure 3 (continued): Panels (d–f): carbon, normal-steel and tight-weave-steel TRM. Each panel retains its own numerical colourbar.

Table 2: Numerical colourbar extrema at the displayed output states.

System	Textile	PEEQ extremum	DAMAGET extremum
TR-EGC	C	3.495×10^{-4}	0.3752
TR-EGC	S	3.394×10^{-5}	0.3709
TR-EGC	TS	3.105×10^{-4}	0.3732
TRM	C	4.303×10^{-4}	—
TRM	S	3.573×10^{-5}	—
TRM	TS	3.433×10^{-5}	—

Values are read from the individual colourbars and are not extrema over complete loading histories. TRM DAMAGET fields are not supplied, and identical output states are not assumed.

Table Abbreviations: TR-EGC, textile-reinforced engineered geopolymer composite; TRM, textile-reinforced mortar; C, carbon textile; S, normal-steel textile; TS, tight-weave-steel textile; PEEQ, Abaqus equivalent plastic strain output identifier; DAMAGET, Abaqus tensile damage variable.

The colourbar readings set limits on amplitude comparisons. In TR-EGC, the displayed extrema for C, S and TS are 3.495×10^{-4}, 3.394×10^{-5} and 3.105×10^{-4}, respectively. The normal-steel value is approximately one order of magnitude lower than the other two. Carbon and tight-weave steel have similar extrema but different spatial distributions. In TRM, the corresponding values are 4.303×10^{-4}, 3.573×10^{-5} and 3.433×10^{-5}. The TS amplitude changes substantially between the two matrices, but a quantitative link to matrix toughening requires comparison at aligned output states.

These fields suggest that textile architecture and matrix response jointly affect the spatial constraints on local deformation. A denser grid may add transfer paths while increasing local constraint at crossings or clamping transitions. Greater spatial dispersion does not necessarily reduce the maximum value. Since the constitutive meaning of PEEQ depends on the material model, the distributions are interpreted as numerical evidence of local non-uniformity. They do not substitute for tensile plastic strain or crack opening.

Magnitude and position of tensile damage

Figure 4 shows DAMAGET for the three TR-EGC systems. The carbon-textile case has a broad central damaged region. The normal-steel and tight-weave-steel cases show more distinct upper and lower regions, with lower damage between them. These patterns describe the spatial shape of the displayed dt field. They neither identify a discrete crack surface nor establish that the band geometry persists throughout loading.

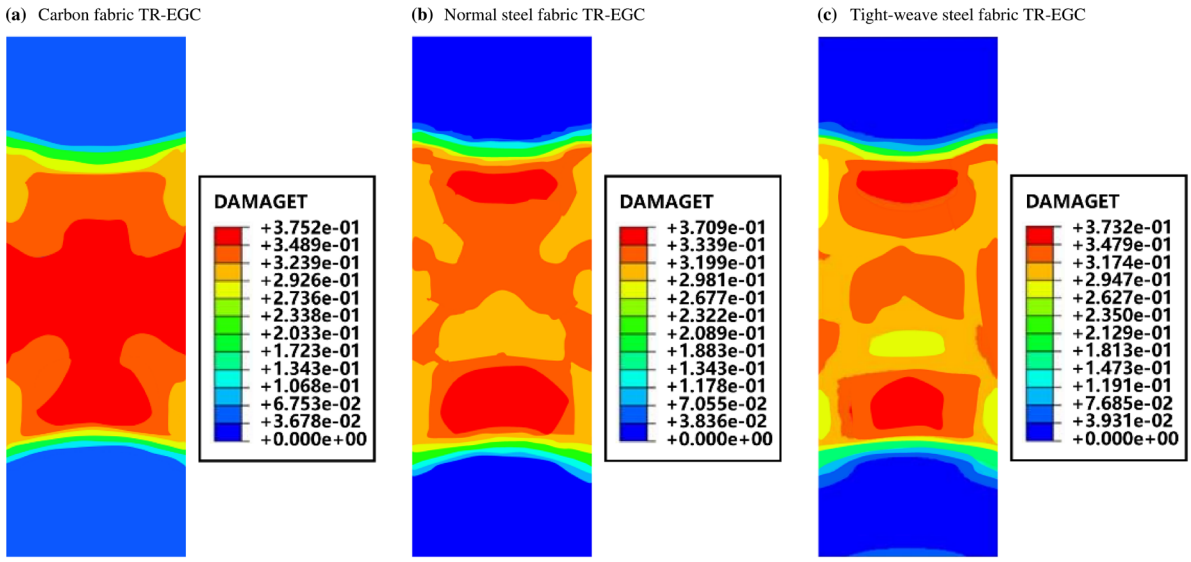


Figure 4: DAMAGET fields from the simulations: (a) carbon-textile TR-EGC; (b) normal-steel TR-EGC; (c) tight-weave-steel TR-EGC. The colourbars represent tensile damage at the displayed output states, not crack opening or dissipated energy.

The displayed DAMAGET extrema are 0.3752, 0.3709 and 0.3732. Their absolute spread is 0.0043, approximately 1.2% of the smallest value. Architecture-dependent differences are clearer in the position and width of the damaged regions than in the maximum damage variable. Normal steel has the lowest extremum and tight-weave steel the intermediate value. This ranking and the damage-band geometry describe different aspects of the response. Assessing physical damage or dissipation capacity also requires aligned output states and spatial or history-dependent measures.

Relation between load capacity and local variables

Figures 2–4 address three distinct questions: how well the model reproduces the structural response, where non-uniform deformation concentrates, and whether the outputs establish a specific crack or interface-failure mechanism. The curves provide graphical evidence for structural agreement, while PEEQ and DAMAGET locate non-uniform material responses. Establishing the failure mechanism also requires crack-surface displacement, interface slip or crack-specific outputs. The results do not establish a monotonic relationship between higher load capacity and a smaller local output variable.

Mechanical interpretation and scope

Competition between textile bridging and interfacial slip offers a physical explanation for the differences between structural responses and local fields. Sufficient interface constraint transfers force to the textile after matrix cracking, but concentrated constraint can confine deformation to a short region. Multiple-fracture theory and interfacial fracture analysis relate transfer length, interface state and matrix fracture resistance [1,2]. The architecture-dependent fields are consistent with this explanation, although the snapshots do not isolate each factor's contribution.

Discretisation and output processing also affect comparisons of local variables. Quasi-brittle softening requires suitable energy regularisation and adequate resolution near cracks; XFEM retains both requirements [13,12]. The nodally averaged display in Figure 3 means that the mesh and averaging procedure can influence both extrema and apparent band widths. The architecture comparisons are therefore confined to the calculations and output states shown. They do not establish a mesh-independent material law.

This assessment does not report mesh-refinement error, local-field measures at a common displacement, or separate dissipation histories for matrix cracks and textile interfaces. Close peak loads are therefore insufficient to validate the crack-growth mechanism fully. A stronger test would align the loading state with crack-specific outputs and energy measures. Further contour plots for different architectures alone would not resolve the issue. This additional

evidence is needed to distinguish parameter non-uniqueness from a physical effect of textile architecture.

Conclusion

This study assessed structural load–elongation responses and local material outputs separately using an extended finite element and interfacial load-transfer description. Peak differences in the six plotted responses are a few percent, while post-peak discrepancies vary with textile architecture. Agreement near the peak constrains load capacity but does not uniquely identify the contributions of matrix softening, interface slip and crack growth.

PEEQ and DAMAGET describe different constitutive quantities. The displayed PEEQ extremum for normal-steel TR-EGC is approximately one order of magnitude below those for carbon and tight-weave steel. By comparison, the three DAMAGET extrema lie within 0.3709–0.3752. The evidence supports architecture-dependent changes in the location and spatial organisation of localisation more directly than a universal performance ranking based on the maximum of a local output variable.

Structural agreement, material-point damage and discrete crack geometry each require distinct evidence. For textile-reinforced quasi-brittle composites, loading states must be aligned and examined alongside crack, interface and energy outputs before differences in local fields can be attributed to a testable failure mechanism.

Data Availability

The experimental reference is the published study by Lam and co-workers [11]. The source archive contains the vector figures, recovered graphical coordinates, colourbar readings, plotting code and analysis script used in this manuscript. It does not include Abaqus input files or output databases. Recovered graphical coordinates reproduce the manuscript figures but do not replace experimental sampling records or finite element integration-point data.

Acknowledgements

This work is financially supported by the National Natural Science Foundation (No. 12004285), Guangdong Provincial Educational Research Project (No. 2022GXJK352), Jiangmen City Social Development Field Science and Technology Plan Project (No. 2024800100180007805).

Conflict of Interest

The authors declare no competing interests related to this work.

Appendix A: Stress definitions and supplementary responses

Textile material stress and composite nominal stress are defined using different cross-sectional areas in Eq. (A1). The supplementary response uses an effective normal-steel textile area of At=4.24 mm^2 and a gross S-4 specimen area of Ag=50 mm×10 mm=500 mm^2. For a shared force record, At/Ag=0.00848 converts algebraically between the stress definitions. This factor alone does not establish that two stress curves derive from the same force record.

$$\sigma_t = \frac{P}{A_t}, \sigma_{\text{nom}} = \frac{P}{A_g}, \sigma_{\text{nom}} = \frac{A_t}{A_g}\sigma_t \qquad \text{(A1)}$$

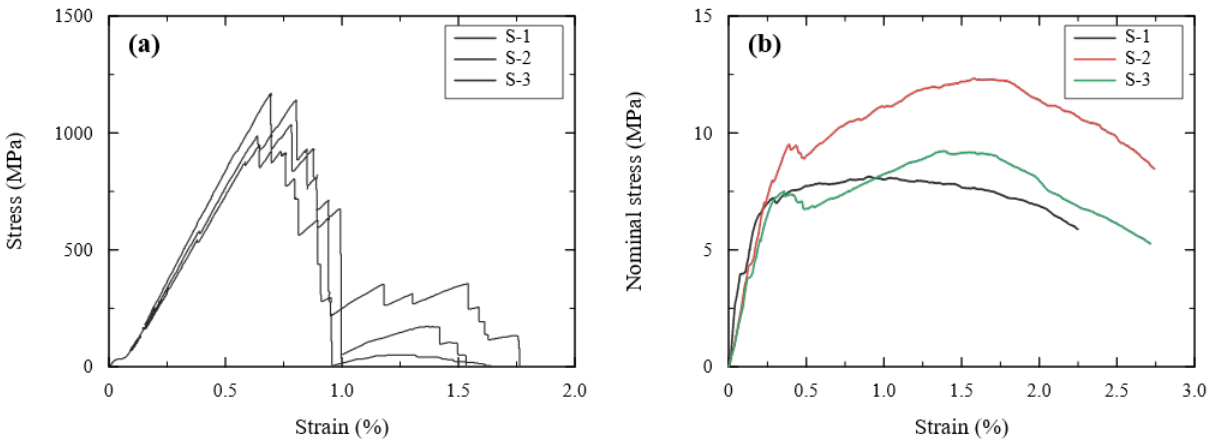


Figure A1: Supplementary stress responses: (a) normal-steel textile material stress, normalised by 4.24 mm^2; (b) S-4 composite nominal stress, normalised by 500 mm^2. S-1 to S-3 denote three specimen records. The panels use different physical definitions of stress.

Figure A1 presents the textile response separately from the S-4 composite nominal-stress response. The two panels use different stress definitions, so their peak values are not directly comparable. Strain is the nominal strain reported in the supplied test record; the main-text model assessment consistently uses force and elongation. Classical multiple-fracture theory provides a physical basis for post-cracking bridging [1], but it is not used here to identify interface parameters independently.

References

1. Aveston J, Kelly A (1973) Theory of multiple fracture of fibrous composites. J Mater Sci 8(3): 352–362.
2. Budiansky B, Hutchinson JW, Evans AG (1986) Matrix fracture in fiber-reinforced ceramics. J Mech Phys Solids 34(2): 167–189.
3. Ohno M, Li VC (2018) An integrated design method of Engineered Geopolymer Composite. Cem Concr Compos 88: 73–85.
4. Lyu BC, Ding C, Guo LP, Chen B, Wang Ag (2021) Basic performances and potential research problems of strain hardening geopolymer composites: A critical review. Constr Build Mater 287: 123030.
5. Truong VD, Kim DJ (2021) A review paper on direct tensile behavior and test methods of textile reinforced cementitious composites. Compos Struct 263: 113661.
6. Cai J, Pan J, Han J, Wang X (2022) Mechanical Behaviors of Metakaolin-Based Engineered Geopolymer Composite under Ambient Curing Condition. J Mater Civ Eng 34(7): 04022152.
7. Melenk J, Babuška I (1996) The partition of unity finite element method: Basic theory and applications. Comput Methods Appl Mech Eng 139(1-4): 289–314.
8. Moës N, Dolbow J, Belytschko T (1999) A finite element method for crack growth without remeshing. Int J Numer Methods Eng 46(1): 131–150.
9. Hillerborg A, Modéer M, Petersson PE (1976) Analysis of crack formation and crack growth in concrete by means of fracture mechanics and finite elements. Cem Concr Res 6(6): 773–781.
10. Wang X, Ghiassi B, Oliveira DV, Lam C (2017) Modelling the nonlinear behaviour of masonry walls strengthened with textile reinforced mortars. Eng Struct 134: 11–24.
11. Lam CC, Gu J, Wang X, Cai J (2023) Tensile Behaviors of Textile Grid–Reinforced Engineered Geopolymer Composites. J Mater Civ Eng 35(8): 04023227.
12. Dassault Systèmes (2025) Modeling discontinuities as an enriched feature using the extended finite element method. Abaqus 2025 Documentation. (accessed 28 October 2026).
13. Bažant ZP, Oh BH (1983) Crack band theory for fracture of concrete. Mater Struct 16(3): 155–177.
14. Dassault Systèmes (2025) Concrete damaged plasticity. Abaqus 2025 Documentation. (accessed 28 October 2026).